7
Synthesis, Structure and Antibacterial Properties of Di-, Tetra- and Hexanuclear Organostannoxanes

Research Article based on this study:

Mishra, A., Batar, A., Kumar, R., Khandelwal, A., Lama, P., Chhabra, M., and Metre, R. K., (2021), "Assembly of Di-, Tetra- and Hexanuclear Organostannoxanes Using Hemi Labile Intramolecular N→Sn Coordination: Synthesis, Structure, DFT and Antibacterial Studies", *Polyhedron*, Vol.209, p.115487.

7.1 Introduction

The modification with substituents on metal centers as well as coordinating ligands in main-group organometallic complexes has given a new direction to generate complexes having novel structures with diverse properties [Dehnen et al., 2007; Kundu, 2020; Wilson et al., 2019]. Organotin complexes have been explored boundlessly for their diverse structure [dos Santos et al., 2020] as well as their potential applications in area of optoelectronics [Hamui et al., 2021], memristive devices [Mishra et al., 2020], functional materials [Rosemann et al., 2016a], catalysis [Paquin et al., 2013], negative differential resistance [Mishra et al., 2021b] and biologically active agents [Mishra et al., 2021c; Wang et al., 2017a] etc. Among all the known organotin complexes, organostannoxanes have been found to show fascinating structures such as drum, ladder, o-capped cluster, cube, double cube, crown cluster, butterfly cluster, extended cluster etc [Chandrasekhar et al., 2002b]. These structures have also gained interest preferentially because of their supramolecular architectures in the solid-state [Chandrasekhar et al., 2002a; Kundu et al., 2015b, 2016].

Organotin carboxylates, comprised of an important class of organostannoxanes, have been a subject of intensive research in the last few decades [Chandrasekhar et al., 2002b; Tiekink, 1991]. Carboxylate ligands have the advantage of acting as multicoordination site ligands and can act as monodentate, bridging bidentate or isobidentate ligands resulting in diverse structures [Chandrasekhar et al., 2013a; Sirajuddin et al., 2019]. Among different strategies available, variation in the structure of these complexes can also be achieved by changing different organic substituents attached to the tin center [Mishra et al., 2020; Rosemann et al., 2016a]. Organotin carboxylates have been particularly investigated widely for their applications in areas of biological activity such as antibacterial, antitumor, and anticancer activity [Hadi et al., 2019]. Salam *et al.* has reported a mono and a few diorganotin derivatives of 2-hydroxyacetophenone-2-methylphenylthiosemicarbazone, out of which diorganotin derivative exhibited better antibacterial activity against S. aureus, E. aerogenes, E. coli, and S. typhi [Salam et al., 2012]. Recently, Zhang *et al*. have reported a cyclometallated iridium(III)-triorganotin(IV) carboxylate, which undergoes three-photon absorption and shows considerable antibacterial activity against Staphylococcus aureus bacteria [Zhang et al., 2020]. Hu *et al.* have reported two triorganotin carboxylates derived from coumarin functionalized carboxylic acid that showed excellent antibacterial activity towards E. coli and B. subtilis bacteria [Hu et al., 2018].

Hexanuclear organostannoxanes with drum structure are known in the literature for their potential applications in various fields. Sharps *et al.* reported a drum structure decorated with an n-butyltin center as a photoresist for lithography and direct-write functional nanomaterial for nanopatterning [Sharps et al., 2019]. Guan *et al.* have reported a drum structure obtained with 3-(3-ethoxy-4-(2-(2-methoxyethoxy)ethoxy)phenyl)acrylate ligand, which showed two-photon excited fluorescence and promising anticancer activity [Guan et al., 2018]. Xiao *et al.* has reported a luminescent organotin drum functionalized with a carbazole ligand [Xiao et al., 2019]. Unlike monoorganostannoxanes with drum structures, other structural forms such as diorganotin macrocycle and unsupported dinuclear monoorganostannoxanes with RSn-O-SnR motif are very scarcely reported in the literature.

Intramolecular N→Sn coordination appears to play an important role in stabilizing unique structural forms, particularly amongst monoorganostannoxanes. So far, there are only two monoorganotin carboxylate structures reported in the literature; $[(RSn)_2(\mu_2\text{-}O)(\mu_2\text{-}FcCOO)_2(\eta\text{-}FcCOO)_2]$ (R=2-phenylazophenyl, Fc=ferrocenyl-) and $[\{L^{CN}Sn(OC(O)CF_3)\}_2(\mu\text{-}O)(\mu\text{-}OC(O)CF_3)_2]$ {L^{CN}= 2-(N,N-dimethylaminomethyl)phenyl-)} bearing RSn-O-SnR motif stabilized via N→Sn intramolecular coordination [Chandrasekhar et al., 2013a; Švec et al., 2011]. The use of intramolecular coordination strategy to stabilize unique structural motifs is well documented amongst transition as well as main group metal complexes. Some of the representative examples from organotin complexes reported in the literature are shown in Chart 7.1 [Bouška et al., 2012, 2018; Mairychová et al., 2013; Mishra et al., 2021b; Švec et al., 2011].

Herein, we report the chemistry of organotin complexes containing hemilabile intramolecular N→Sn coordination. We report the synthesis, structural characterization, DFT studies, and antibacterial activity of a hexanuclear monoorganostannoxane $[RSn(\mu_2\text{-}O)(\mu_2\text{-}O_2CPh]_6{\cdot}4PhCH_3$ **(5)**, a dinuclear monoorganostannoxane $[(RSn)_2(\mu_2\text{-}O)(\mu_2\text{-}O_2CPh)_2(\kappa^2\text{-}O_2CPh)_2]{\cdot}PhCH_3$ **(6)** and a tetranuclear diorganotin macrocycle $[R_2Sn(\mu_2\text{-}O)]_4$ **(7)** (R = 2-phenylazophenyl).

Chart 7.1 Representative examples of intramolecularly stabilized organotin complexes reported in the literature [Bouška et al., 2012, 2018; Mairychová et al., 2013; Mishra et al., 2021b; Švec et al., 2011].

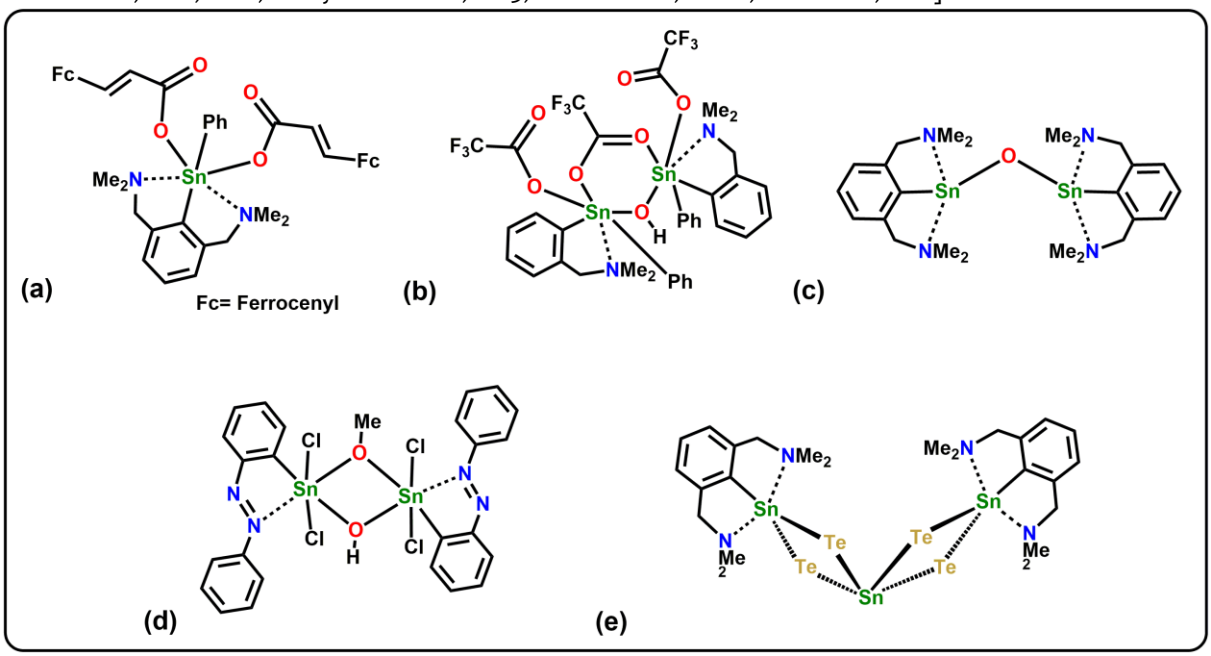

7.2 Experimental Section

7.2.1 Synthesis

[RSn(O)(OH)]$_n$ (R = 2-phenylazophenyl) (A). A suspension of $RSnCl_3$ (100 mg, 0.246 mmol) and sodium hydroxide (30 mg, 0.75 mmol) in 30 ml ethanol/water (1:1) was taken in a round bottom flask equipped with a reflux condenser. The mixture was heated to reflux for 8 h. The

mixture was allowed to cool and then filtered. The precipitate obtained was washed with water and hexane to remove starting materials and air-dried. (2-phenylazophenyl)stannoic acid (**A**) thus obtained was used for further reactions. Yield (Based on Sn): 0.05g (61%). M.P. > 190ºC (decomp.); ^{119}Sn NMR (186MHz, $CDCl_3$, ppm): δ -533.

[RSn(μ$_2$-O)(μ$_2$-O$_2$CPh]$_6$·4PhCH$_3$ (R = 2-phenylazophenyl) (5). A mixture of **A** (100 mg, 0.3 mmol) and benzoic acid (36.6 mg, 0.3 mmol) in 20 ml dry toluene was heated under reflux for 8 h. The resultant clear yellow-orange solution was allowed to cool and then filtered. Slow evaporation of the filtrate gave orange colored x-ray quality crystals after few weeks. Yield (Based on Sn): 0.08g (61%). M.P. > 230ºC (decomp.); Anal. calcd for $C_{114}H_{84}N_{12}O_{18}Sn_6$ C, 52.22; H, 3.23; N, 6.41 Found: C, 52.36; H, 3.00; N, 6.64. ^{1}H NMR (500MHz, $CDCl_3$, ppm): δ 8.65 (d), 8.26 (d), 8.11 (d), 7.73 (d), 7.65 (d), 7.46 (d), 7.1 (m), 6.6 (m), 6.4 (m), 6.3 (m). ^{13}C{^{1}H}NMR (125MHz, $CDCl_3$, ppm):δ 172, 155, 152, 147, 137, 132, 131, 130, 129, 128, 127, 123, 114. ^{119}Sn NMR (186MHz, $CDCl_3$, ppm): δ -546. IR (KBr, cm^{-1}): 3444 (br), 3062 (w), 2918 (w), 2849 (w), 1598 (s), 1446 (w), 1413 (m), 1378 (s), 1103 (w), 776 (s), 688 (s), 568 (s).

[(RSn)$_2$(μ$_2$-O)(μ$_2$-O$_2$CPh)$_2$(κ^2-O$_2$CPh)$_2$]·PhCH$_3$ (R = 2-phenylazophenyl) (6). A mixture of **A** (0.1 g, 0.3 mmol) and benzoic acid (0.074 g, 0.6 mmol) in 20 ml dry toluene was heated under reflux for 8 h. The obtained clear solution was filtered and kept for complete evaporation, as a result of which yellow solid was collected. The solid was washed with water and hexane and dissolved in the mixture of chloroform and toluene (1:1). X-ray quality crystals of **2** were grown by the slow evaporation of the mixture of the solvents. Yield (Based on Sn): 0.09g (55%). M.P. >210ºC (decomp.); Anal. calcd for $C_{52}H_{38}N_4O_9Sn_2$ C, 56.76; H, 3.48; N, 5.09; Found: C, 56.21; H, 3.05; N, 5.38. ^{1}H NMR (500MHz, $CDCl_3$, ppm): δ 8.64 (s), 8.25 (d), 8.17 (s), 7.88 (s), 7.68 (d), 7.46 (s), 7.26 (m), 7.17 (m). ^{13}C{^{1}H}NMR (125MHz, $CDCl_3$, ppm):δ 148, 137, 133, 130, 129, 128.37, 128, 125. ^{119}Sn NMR (186MHz, $CDCl_3$, ppm): δ -636. IR (KBr, cm^{-1}): 3058 (w), 1599 (m), 1554 (m), 1406 (s), 1171 (w), 770 (m), 719 (m), 684 (m).

[R$_2$Sn(μ$_2$-O)]$_4$ (R = 2-phenylazophenyl) (7). NaOH (22 mg, 0.55 mmol) was added to a clear solution of R_2SnCl_2 (R = 2-phenylazophenyl) (150 mg, 0.27 mmol) in 20 ml of acetone/methanol (1:1) and the suspension was stirred at room temperature for 4 h. The clear orange solution was filtered and kept for complete evaporation. The orange solid obtained was dissolved in dichloromethane and x-ray quality crystals were collected after few days by the slow diffusion of hexane into dichloromethane solution. Yield (Based on R_2SnCl_2): 0.11 g (81%). M.P. >230º C (decomp.); Anal. calcd for $C_{96}H_{72}N_{16}O_4Sn_4$ C, 57.98; H, 3.65; N, 11.27; Found: C, 58.14; H, 3.63; N, 10.63. ^{1}H NMR (500MHz, $CDCl_3$, ppm): δ 8.27 (s), 7.6 (m), 7.39 (d), 7.2 (d), 7.04 (m), 6.92 (m). ^{13}C{^{1}H}NMR (125MHz, $CDCl_3$, ppm): δ 137, 136, 130, 129, 128, 123,. ^{119}Sn NMR (186MHz, $CDCl_3$, ppm): δ -211; IR (KBr, cm^{-1}): 3435 (br), 3051 (w), 2931 (w), 1608 (m), 1408 (w), 772 (s), 681 (m), 531 (w).

7.2.2 Single-Crystal X-ray Crystallography

The details pertaining to the data collection and refinement for **5**, **6** & **7** are given in Table 7.1. As the solvent molecules in **5** and **6** were disordered with high thermal factor values even at 100 K, squeeze analysis was performed using Program PLATON [Spek, 1999] and the squeeze result was appended to the CIF file. The squeeze analysis shows that there are 812 electrons present per unit cell (Z=4) in 5 assigned to four Toluene molecules, whereas 204 e per unit cell (Z=4) in 6 assigned to one Toluene molecule.

Table 7.1 Crystal data and structure refinement parameters for complexes **5-7**.

Identification code	**5**	**6**	**7**
Empirical formula	$C_{142}H_{116}N_{12}O_{18}Sn_6$	$C_{59}H_{46}N_4O_9Sn_2$	$C_{96}H_{72}N_{16}O_4Sn_4$
Formula weight	2990.81	1192.46	1988.58
Temperature/K	100(2)	100(2)	100(2)

Crystal system	monoclinic	monoclinic	tetragonal
Space group	C2/c	C2/c	$I4_1/a$
a/Å	32.981(15)	15.442(2)	14.223(3)
b/Å	17.574(8)	16.754(3)	14.223(3)
c/Å	23.322(11)	19.471(3)	41.940(8)
α/°	90	90	90
β/°	95.944(7)	95.406(2)	90
γ/°	90	90	90
Volume/$Å^3$	13445(10)	5015.1(13)	8485(3)
Z	4	4	4
$\rho_{calc}g/cm^3$	1.295	1.457	1.557
μ/mm^{-1}	1.156	1.054	1.227
F(000)	5184.0	2200.0	3968.0
Crystal size/mm^3	0.220 × 0.160 × 0.120	0.220 × 0.170 × 0.120	0.230 × 0.160 × 0.110
Radiation	MoKα (λ = 0.71073)	MoKα (λ = 0.71073)	MoKα (λ = 0.71073)
2Θ range for data collection/°	2.482 to 49.998	3.596 to 49.996	3.024 to 49.98
Index ranges	-39 ≤ h ≤ 39, 0 ≤ k ≤ 20, 0 ≤ l ≤ 27	-18 ≤ h ≤ 18, -19 ≤ k ≤ 19, -23 ≤ l ≤ 23	-16 ≤ h ≤ 16, -16 ≤ k ≤ 16, -49 ≤ l ≤ 49
Reflections collected	11836	50257	92417
Independent reflections	11836 [R_{int} = 0.0, R_{sigma} = 0.0594]	4430 [R_{int} = 0.0305, R_{sigma} = 0.0125]	3738 [R_{int} = 0.0866, R_{sigma} = 0.0257]
Data/restraints/parameters	11836/0/646	4430/0/303	3738/0/271
Goodness-of-fit on F^2	0.985	1.025	1.098
Final R indexes [I>=2σ(I)]	R_1 = 0.0381, wR_2 = 0.0801	R_1 = 0.0185, wR_2 = 0.0442	R_1 = 0.0423, wR_2 = 0.1257
Final R indexes [all data]	R_1 = 0.0591, wR_2 = 0.0857	R_1 = 0.0202, wR_2 = 0.0457	R_1 = 0.0535, wR_2 = 0.1376
Largest diff. peak/hole / e $Å^{-3}$	0.97/-0.45	0.37/-0.25	0.64/-1.07

7.2.3 Assessment of Antibacterial Activity

The antibacterial activity of all the three complexes was analyzed using the standard Kirby-Bauer disc diffusion protocol [Zafarian et al., 2016]. Briefly, three different concentrations of complexes were taken into account, comprising 10, 15, and 20 mg/ml. Chloroform was used as the solvent, followed by a coating of complexes on a sterilized glass slide (1 cm * 1 cm) using a spin-coater. Prior to use, a hot air gun was utilized for the complete removal of chloroform from the coated surface. Both gram-positive and gram-negative bacteria, along with the standard antibiotics (Kanamycin and Hygromycin), were taken into consideration in the study. *Micrococcus luteus and Escherichia coli* were employed in the investigation as gram-positive and gram-negative bacteria, respectively. The bacterial suspension equivalent to 0.5 McFarland was lawn culture using LB media along with 2% agar. This was followed by incubation of plates for 24 h at 37°C. After 24 h, the zone of inhibition (ZOI) displayed by both antibiotics and complexes was analyzed and measured.

7.2.4 Theoretical Calculations

All the Density Functional Theory (DFT) calculations are performed using Gaussian 09 (Revision D.01) Suite of program [Frisch et al., 2009]. The optimization of the complexes has been performed at TPSSh/def2-SVP(all atoms) level of theory [Dirac, 1929; Mishra et al., 2020, 2021b, 2021d; Perdew et al., 2018; Slater, 1951; Staroverov et al., 2003; Tao et al., 2003]. The

single-point calculation, including chloroform solvent using CPCM model at a higher level of theory TPSSh/def2-TZVP(all atoms) has been used to get better results [Weigend et al., 2005]. Chemcraft software is used for the visualization of the HOMO-LUMO orbital [Zhurko et al., 2009].

7.3 Results and Discussion

7.3.1 Synthetic Aspects

The complete hydrolysis of $RSnCl_3$ (R = 2-phenylazophenyl) using sodium hydroxide in a 1:3 ratio was carried out in refluxing ethanol/water (1:1) mixture to yield (2-phenylazophenyl)stannoic acid $[RSn(O)(OH)]_n$ **(A)** (Scheme 7.1) which was confirmed by ^{119}Sn NMR spectrum that shows a single resonance at δ -533 ppm owing to the presence of hexacoordinated chemically equivalent Sn centers, and the observed chemical shift value is comparable to the previously reported intramolecularly N→Sn coordinated stannoic acid [Bouška et al., 2009]. (2-phenylazophenyl)stannoic acid **(A)** on reaction with benzoic acid in a 1:1 molar ratio afforded a toluene solvated hexanuclear monoorganostannoxane $[RSn(\mu_2\text{-}O)(\mu_2\text{-}O_2CPh]_6{\cdot}4PhCH_3$ **(5)** with a drum-like core. Whereas reaction of (2-phenylazophenyl)stannoic acid **(A)** with benzoic acid in a 1:2 molar ratio afforded a toluene solvated dinuclear monoorganostannoxane $[(RSn)_2(\mu_2\text{-}O)(\mu_2\text{-}O_2CPh)_2(\kappa^2\text{-}O_2CPh)_2]{\cdot}PhCH_3$ **(6)** (Scheme 7.2). On the other hand, the synthesis of tetranuclear diorganostannoxane macrocycle $[R_2Sn(\mu_2\text{-}O)]_4$ **(7)** (R = 2-phenylazophenyl) was achieved by the complete hydrolysis of the diorganotin precursor R_2SnCl_2 in the presence of sodium hydroxide in 1:2 molar ratio in acetone/methanol mixture (Scheme 7.3). The ^{119}Sn NMR spectrum of complex **5-7** shows a single resonance at δ -546, -636, and -211 ppm, respectively, indicating that complex **5-7** each contains six, two, and four chemically equivalent tin atoms, respectively. Observed upfield shift trend in ^{119}Sn NMR chemical shift values of complex **5-7** can be associated with the increase in the number of coordination sites on Sn center in **5-7**. In the ^1H NMR spectrum of complex **5-7**, the signals in the range of δ 6.2 to 8.7 ppm are associated with the aromatic protons (Fig. 7.1-7.3). UV-Vis Spectra were recorded for complexes **5-7** in dichloromethane (DCM) solution (Conc. 10^{-5} M) and found that all the complexes show single absorption maxima at ~330-340 nm.

Thermogravimetric analysis revealed that the complexes **5-7** are stable up to 250°C, 220°C, and 270°C, respectively. The residual yield of the complexes **5-7** at 600°C were found to be 35%, 25%, and 45%, respectively (Fig. 7.4-7.6).

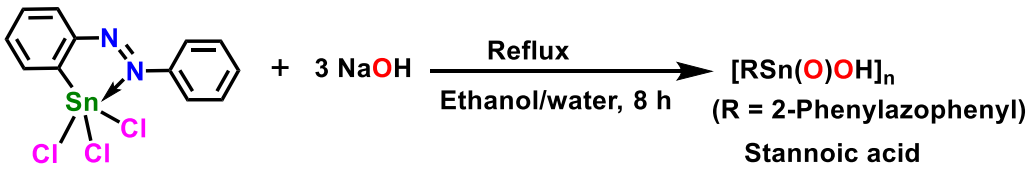

Scheme 7.1 Synthesis of 2-phenylazophenylstannoic acid **(A)** from $RSnCl_3$.

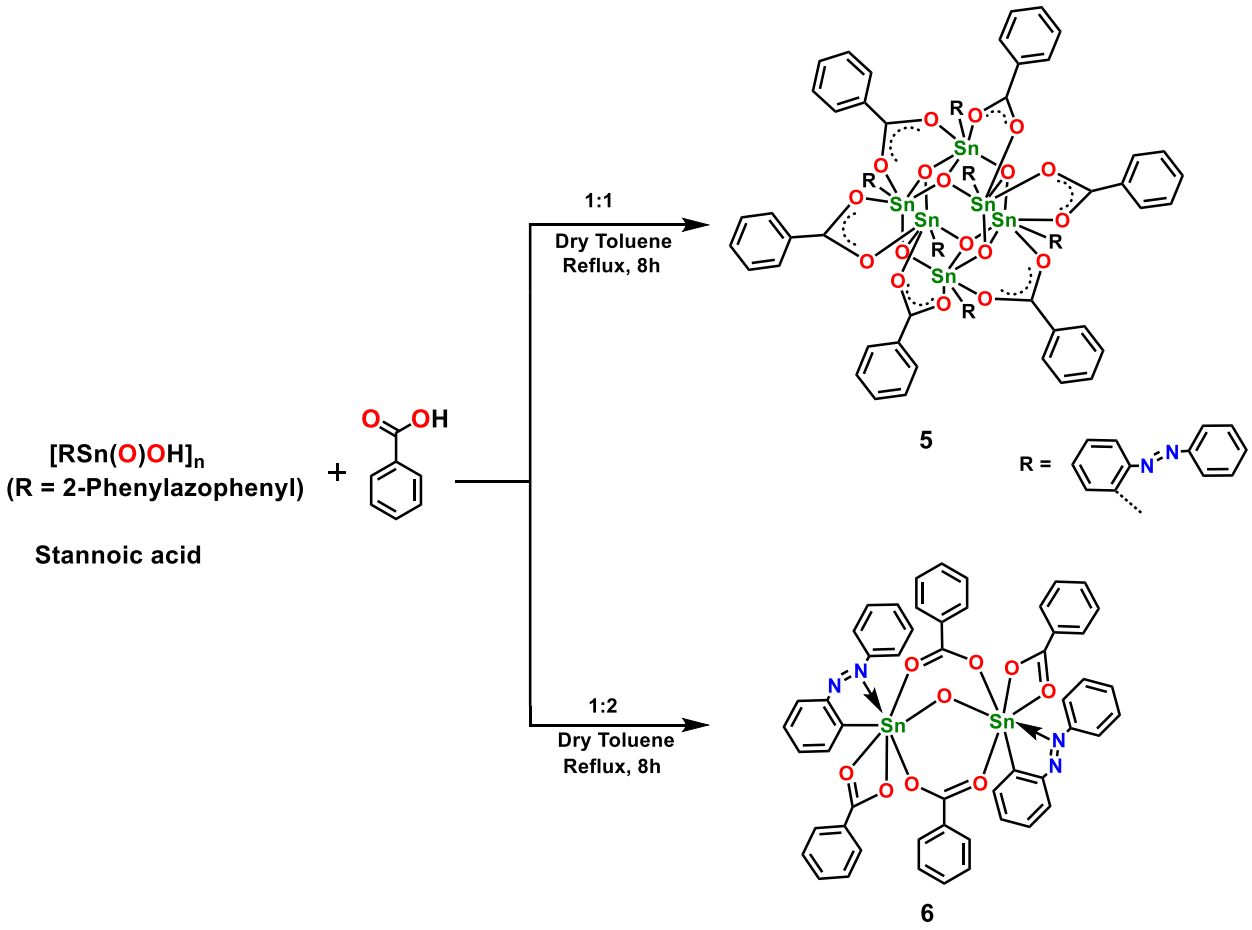

Scheme 7.2 Synthesis of complexes **5** & **6.**

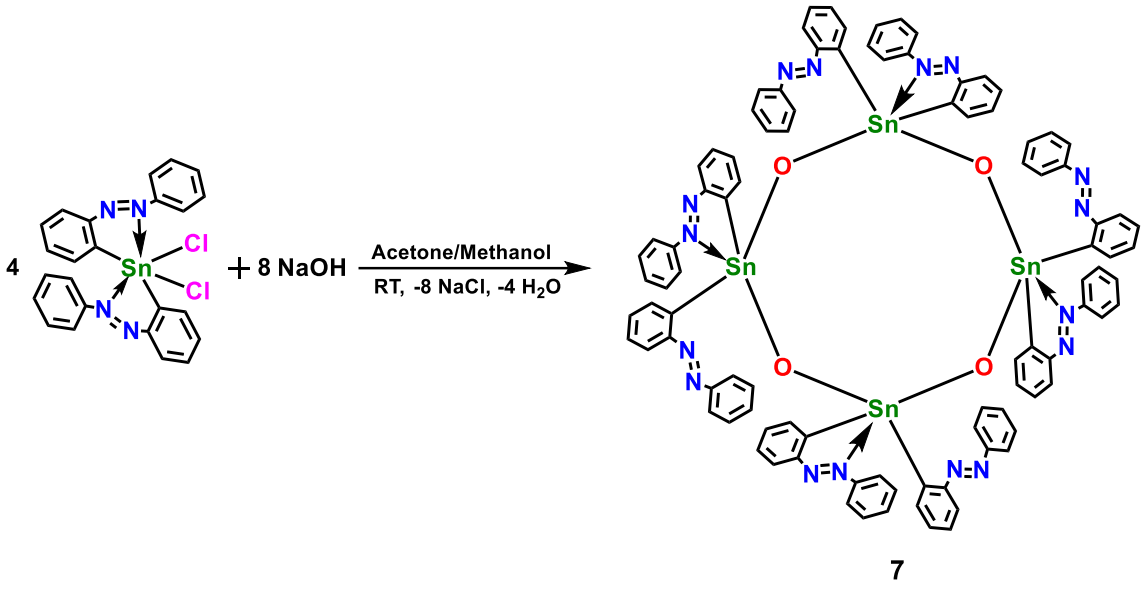

Scheme 7.3 Synthesis of complex **7.**

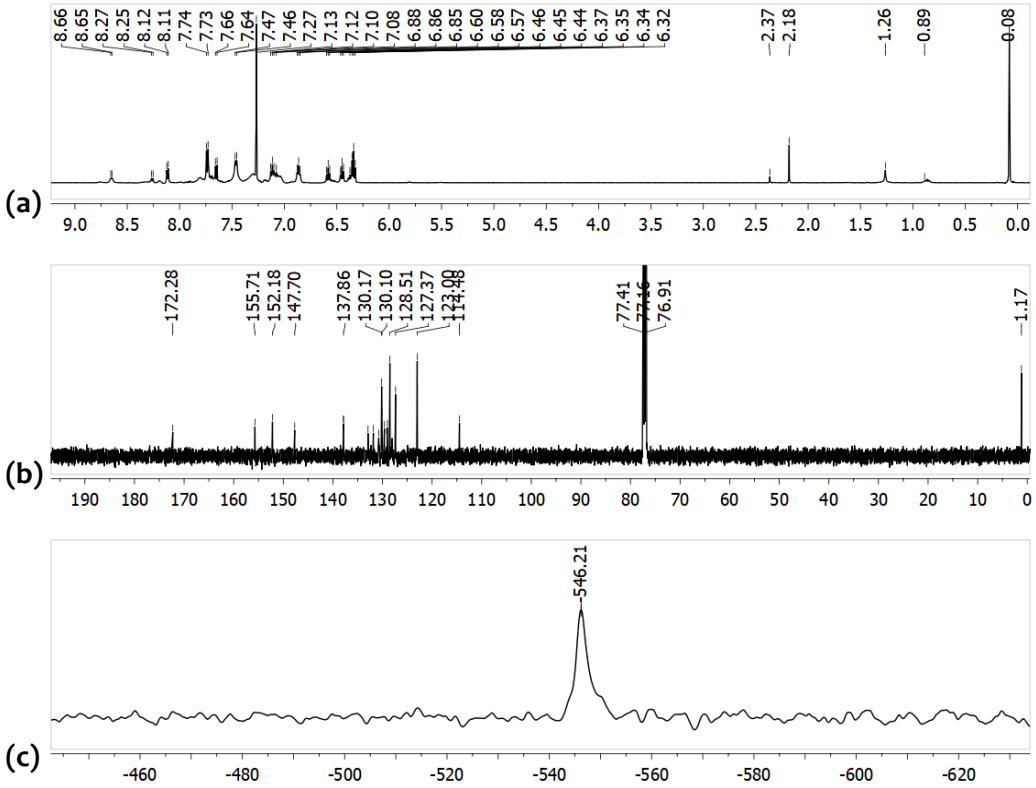

Fig. 7.1 (a) ^{1}H NMR, **(b)** ^{13}C NMR and **(c)** ^{119}Sn NMR of complex **5** recorded in $CDCl_3$.

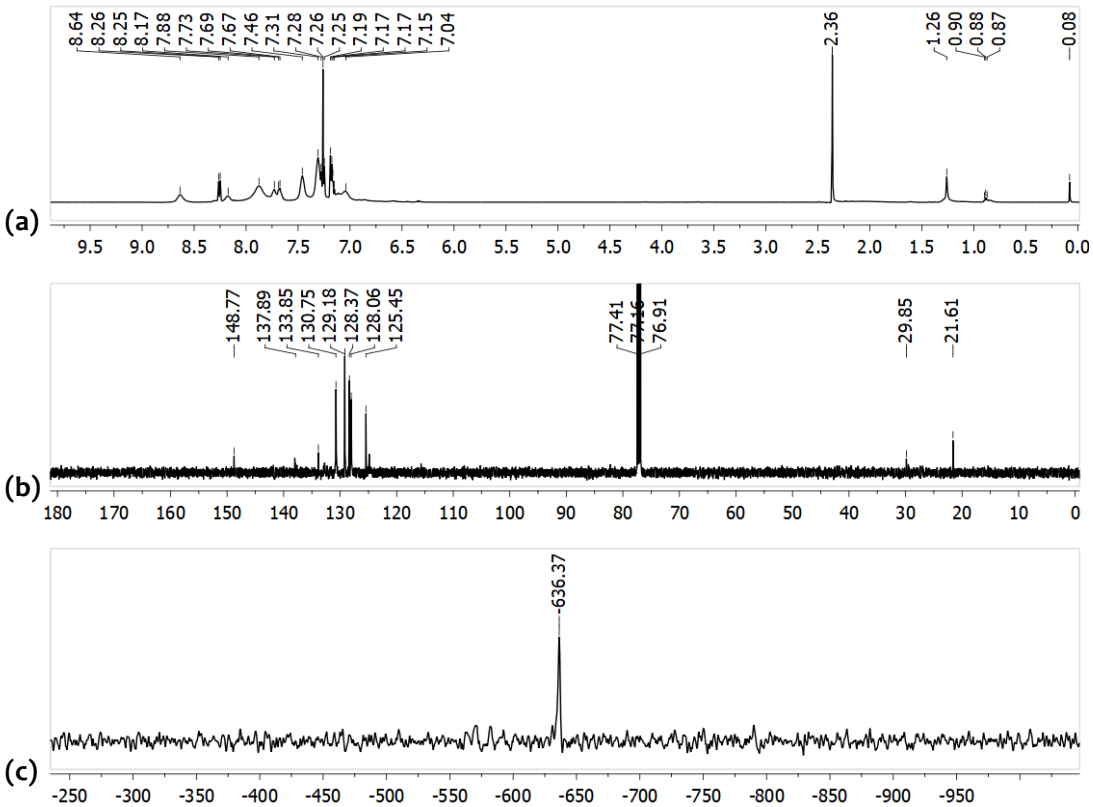

Fig. 7.2 (a) ^{1}H NMR, **(b)** ^{13}C NMR and **(c)** ^{119}Sn NMR of complex **6** recorded in $CDCl_3$.

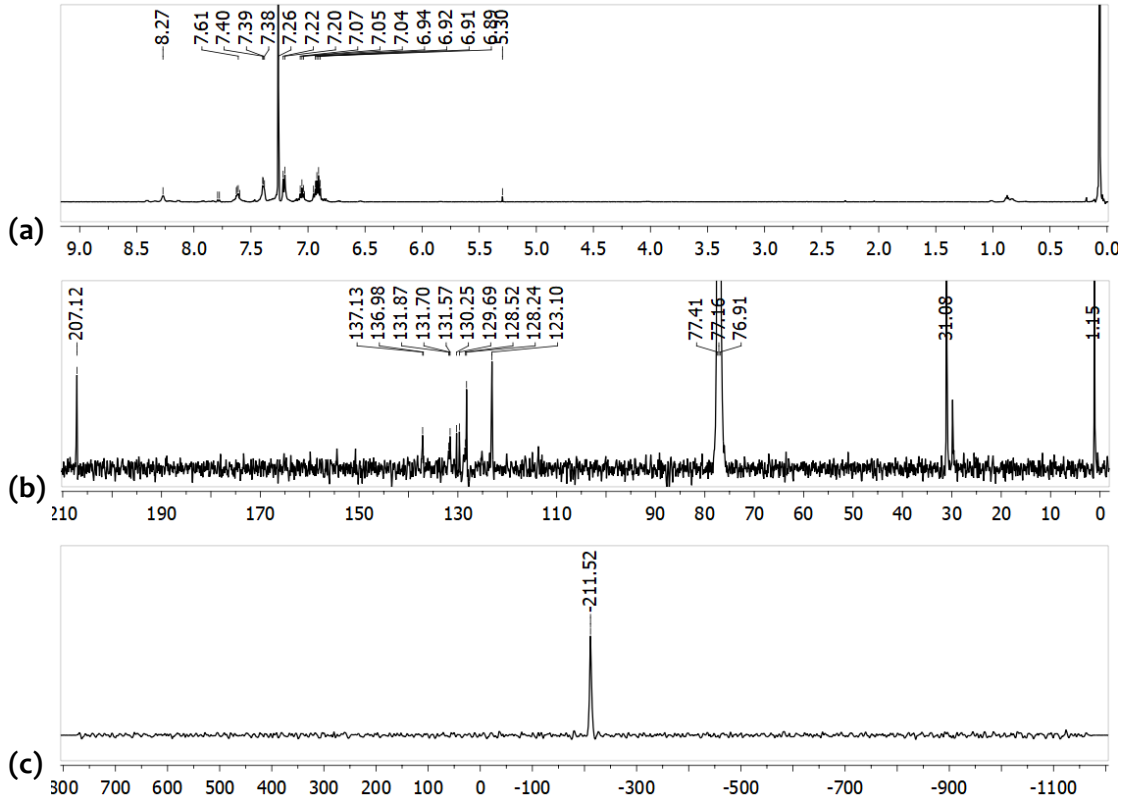

Fig. 7.3 (a) ^{1}H NMR, **(b)** ^{13}C NMR and **(c)** ^{119}Sn NMR of complex **7** recorded in $CDCl_3$.

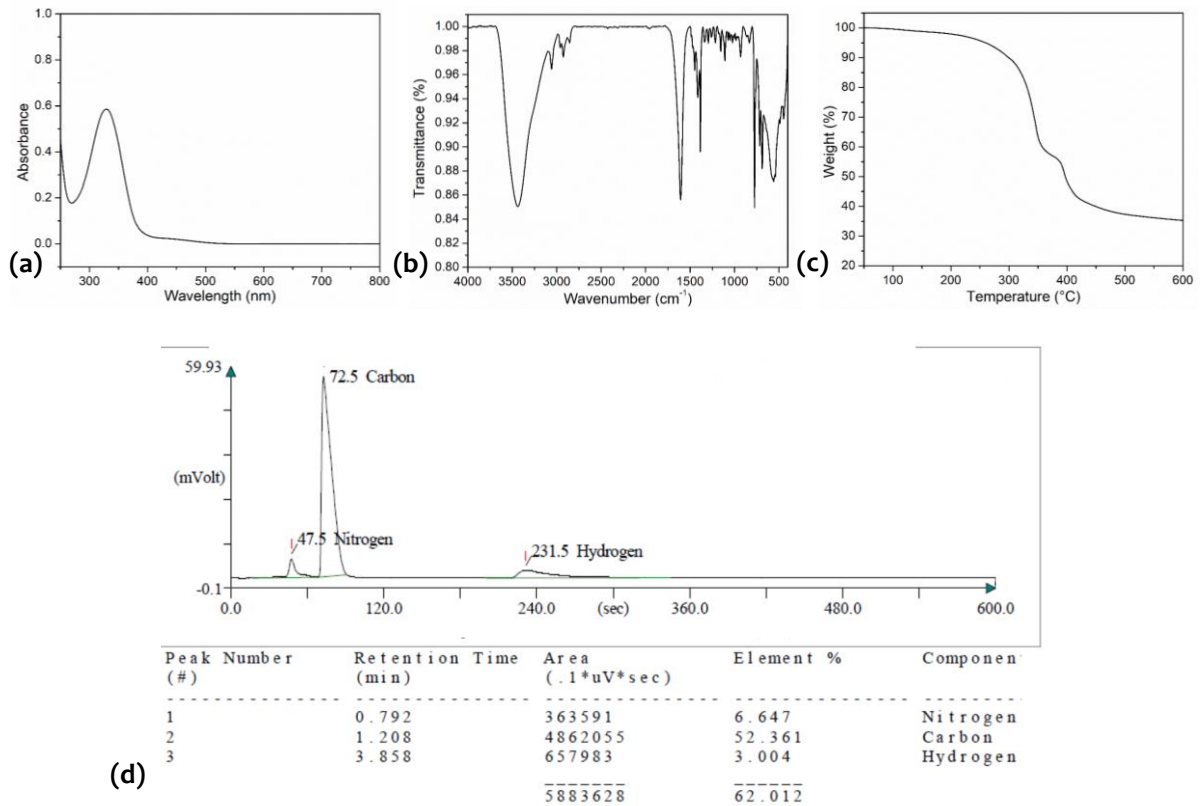

Peak Number (#)	Retention Time (min)	Area (.1*uV*sec)	Element %	Componen
1	0.792	363591	6.647	Nitrogen
2	1.208	4862055	52.361	Carbon
3	3.858	657983	3.004	Hydrogen
		5883628	62.012	

Fig. 7.4 (a) UV-Vis spectrum (conc. 10^{-5}M in DCM), **(b)** FTIR spectrum, **(c)** TGA (under N_2 atmosphere), **(d)** CHN analysis of complex **5**.

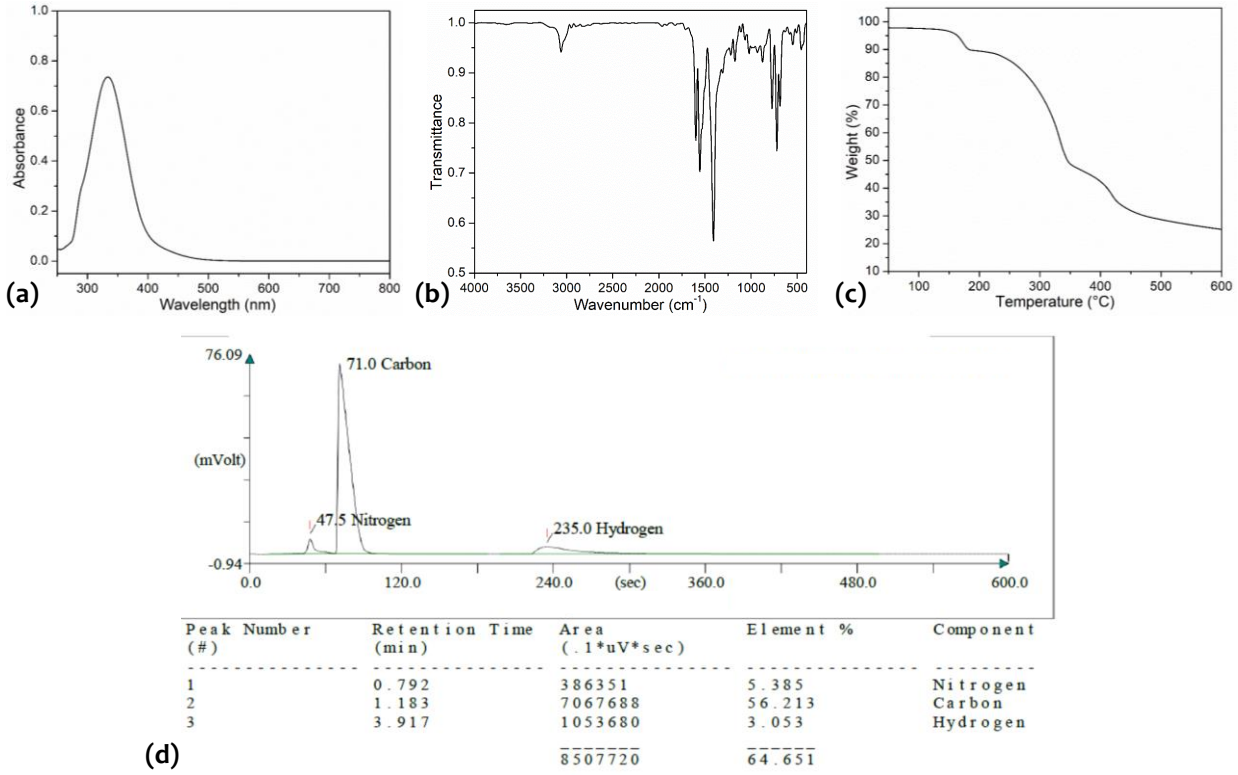

Peak Number (#)	Retention Time (min)	Area (.1*uV*sec)	Element %	Component
1	0.792	386351	5.385	Nitrogen
2	1.183	7067688	56.213	Carbon
3	3.917	1053680	3.053	Hydrogen
		8507720	64.651	

(d)

Fig. 7.5 (a) UV-Vis spectrum (conc. 10^{-5}M in DCM), **(b)** FTIR spectrum, **(c)** TGA (under N_2 atmosphere) **(d)** CHN analysis of complex **6.**

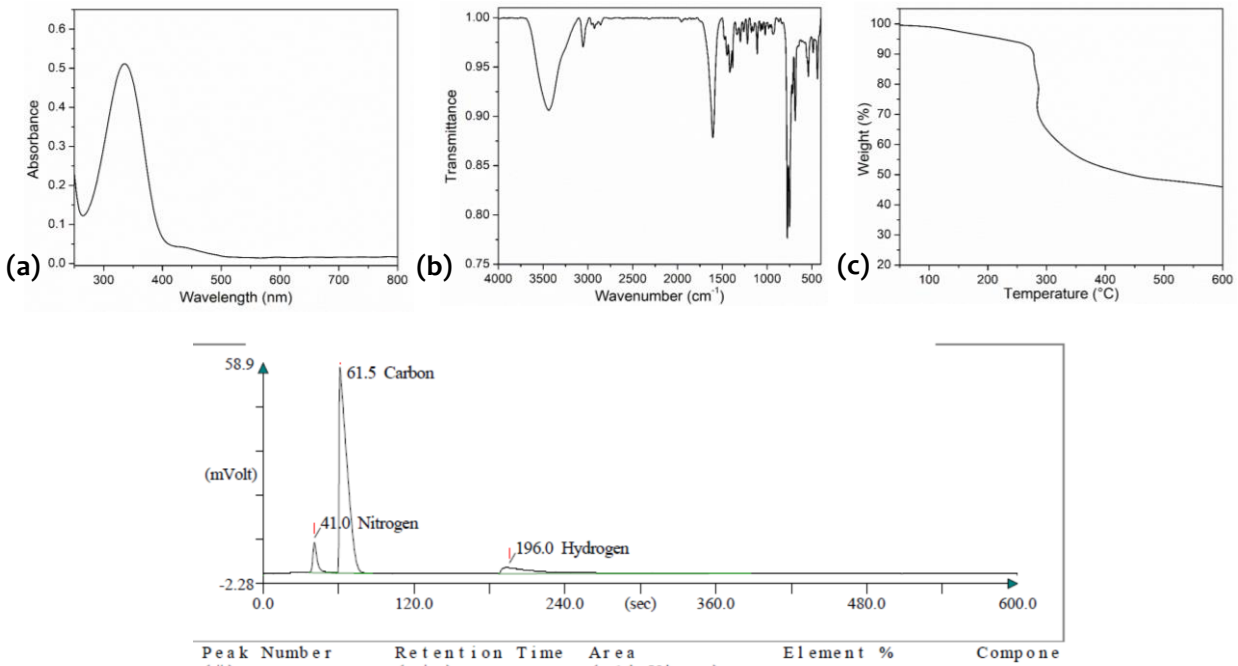

Peak Number (#)	Retention Time (min)	Area (.1*uV*sec)	Element %	Compone
1	0.683	334210	10.635	Nitroge
2	1.025	4080181	58.141	Carbon
3	3.267	611344	3.630	Hydroge
		5025736	72.406	

(d)

Fig. 7.6 (a) UV-Vis spectrum (conc. 10^{-5}M in DCM), **(b)** FTIR spectrum, **(c)** TGA (under N_2 atmosphere) **(d)** CHN analysis of complex **7.**

7.3.2 Molecular and Supramolecular Structures of Complexes 5-7

The molecular structure of complex **5** is shown in Fig. 7.7(a). Closer inspection of the x-ray crystal structure of **5** revealed that complex **5** has a hexanuclear structure having a Sn_6O_6 central drum-like core containing Sn and O atoms at alternate positions. The asymmetric unit consists of six repeating units of [RSn(μ_2-O)(μ_2-O_2CPh); R=2-phenylazophenyl]. A pair of three Sn atoms present on opposite faces are in a plane [Fig. 7.7(b)]. The central core consists of six tin atoms which are bridged by six μ_3-oxo ligands resulting in a drum-like structure. The core contains upper and lower Sn_3O_3 rings, which are held together by six alternate benzoate ligands. Each Sn center is hexacoordinated [5O, 1C coordination] in distorted octahedral geometry with O6' and C1 atoms at axial positions [Fig. 7.7(c)]. It is interesting to note the absence of intramolecular N→Sn coordination in **5,** depicting the hemi-labile nature of N→Sn interaction. The Sn-O bond distances of six-membered Sn_3O_3 rings are Sn(1)-O(3), 2.0707(3)Å, Sn(1)-O(9), 2.0985(3)Å; Sn(2)-O(3), 2.1090(3); Sn(2)-O(6), 2.0694(3)Å; Sn(3)-O(6), 2.0970(2); Sn(3)-O(9), 2.0806(3). The average bond angle of Sn-O-Sn in the upper plane is 133.935°, and O-Sn-O is 102.939°, whereas the bond angle of bridging Sn-O-Sn is Sn(1)-O(6)-Sn(2), 100.622(1)° and O-Sn-O is O(3)-Sn(1)-O(6), 77.695(9)°. The observed bond distances are in well agreement for organostannoxanes with drum structures reported previously in the literature [Guan et al., 2018; Sharps et al., 2019; Xiao et al., 2019].

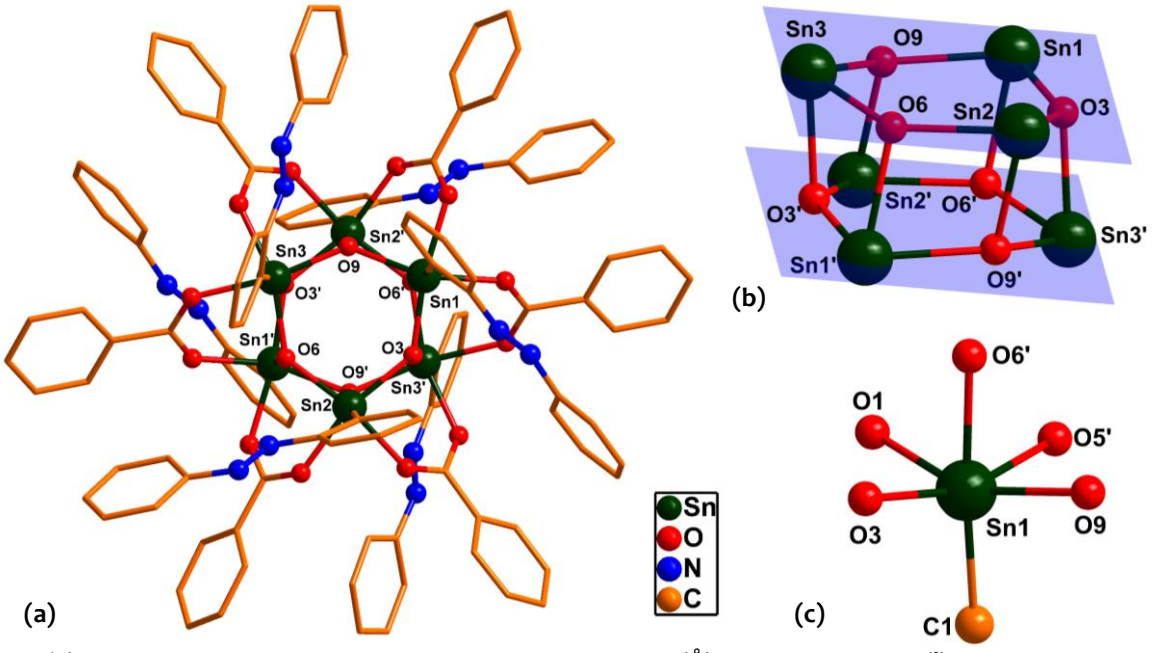

Fig. 7.7 (a) Molecular structure of complex **5.** Bond distance (Å) and bond angle (°) parameters: Sn3-O6, 2.0970(2)Å; Sn3-O3', 2.1109(3)Å; Sn2-O6, 2.0694(3)Å; Sn1-O9-Sn3, 133.850(1)°; Sn1-O3-Sn2, 134.388(1)°, O6-Sn3-O9, 103.509(1)°; Sn2-O9'-Sn1', 99.9(1)°; H atoms are omitted for clarity. **(b)** Core structure with a molecular plane. **(c)** Coordination environment of Sn in complex **5;** Sn1-O3, 2.0707(3)Å; Sn1-O5', 2.1884(3)Å; Sn1-C1; 2.1447(4)Å; Sn1-O1, 2.1427(3)Å; Sn1-O9, 2.0985(3)Å; C1-Sn1-O6', 175.415(1)°; O3-Sn1-O5', 162.269(1)°, O3-Sn1-C1, 106.304(1)°; O5'-Sn1-C1, 88.292(1)°; O1-Sn1-O6', 85.350(1)°.

The molecular structure of complex **6** is shown in Fig. 7.8(a). Closer inspection of the x-ray crystal structure of complex **6** revealed that it has a rare Sn_2O central core in which two Sn atoms (Sn1 and Sn1′) are bridged by μ_2-oxo ligand (Sn1-O5, 1.9455(9)Å; Sn1′-O5, 1.9455(9)Å; Sn1-O5-Sn1′, 123.008(2)°). Apart from μ_2-oxo bridging, both the Sn atoms are further connected through bridging modes of two benzoate ligands. Each Sn atom is also coordinated to one chelating isobidentate benzoate group. Each Sn center is heptacoordinated [5O, 1C, and 1N coordination] with distorted pentagonal bipyramidal geometry with O5 and C1 at axial positions [Fig. 7.8(b)]. The formation of **6** retains the N→Sn intramolecular coordination, and the N→Sn distance found in **6**, 2.437Å; is slightly shorter than that of the starting precursor, 2.451Å [Chandrasekhar et al., 2013a].

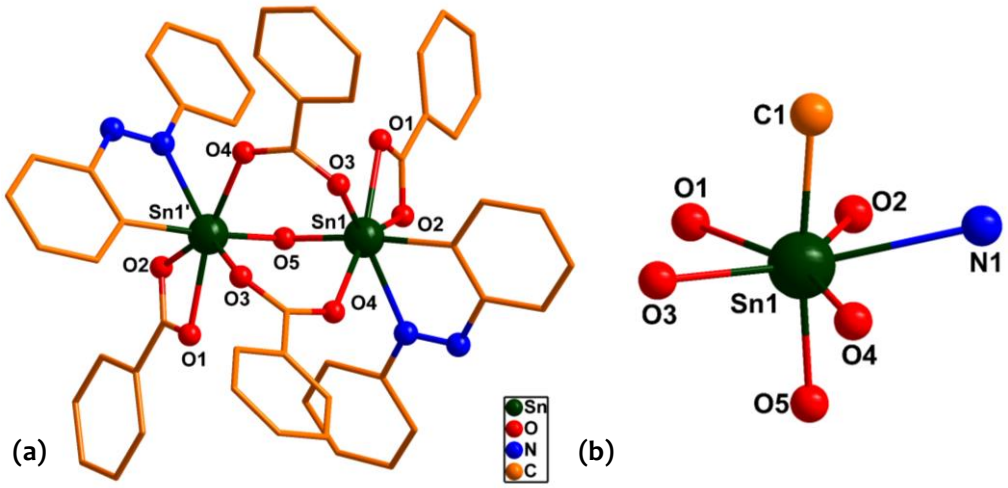

Fig. 7.8 (a) Molecular structure of complex **6**. Bond distance (Å) and bond angle (°) parameters: Sn1-O5, 1.9455(9)Å; Sn1-O1, 2.2794(1)Å; Sn1-O2, 2.2837(1)Å; Sn1-O3, 2.1429(1)Å; Sn1'-O5, 1.9455(9)Å; Sn1-O5-Sn1', 123.008(1)°; H atoms are omitted for clarity. **(b)** Coordination environment of Sn in complex **6**; Sn1-O4, 2.2369(1)Å; Sn1-C1, 2.1092(2)Å; Sn1-N1; 2.4376(2)Å; C1-Sn1-O5, 173.210(5)°, O3-Sn1-N1, 146.398(6)°; O4-Sn1-C1, 89.477(6)°; N1-Sn1-O5, 85.350(1)°; O1-Sn1-O3, 100.371(4)°; C1-Sn1-N1, 72.93(7)°.

The molecular structure of complex **7** is shown in Fig. 7.9(a). Complex **7** is a tetranuclear diorganostannoxane possessing a central cyclic core-forming eight-membered Sn_4O_4 macrocycle. The asymmetric unit consists of four crystallographically unique R_2SnO (R= 2-phenylazophenyl) units. One out of two N→Sn intramolecular coordination is retained during the formation of **7**. All four Sn centers in the central eight-membered cyclic core are present in a boat-like configuration [Fig. 7.9(b)]. The core containing four Sn-O units has the distance; of Sn1-O1, 1.9406(3) Å; Sn1-O1′, 1.9867(3) Å, and the angle Sn1-O1-Sn1‴, 129.396(2)°; O1-Sn1-O1′, 104.482(1)°. The bond parameters of **7** are in close agreement with that of the only similar structure reported in the literature [Padělková et al., 2009]. Each Sn center is pentacoordinated and possesses distorted trigonal bipyramidal geometry with 1N and 1O occupying the axial positions whereas 2C and 1O occupying the equatorial position [Fig. 7.9(c)]. The Addison's tau parameter for complex **7** is found to be τ = 0.56 (τ = 1 for perfect trigonal bipyramidal geometry) [Addison et al., 1984].

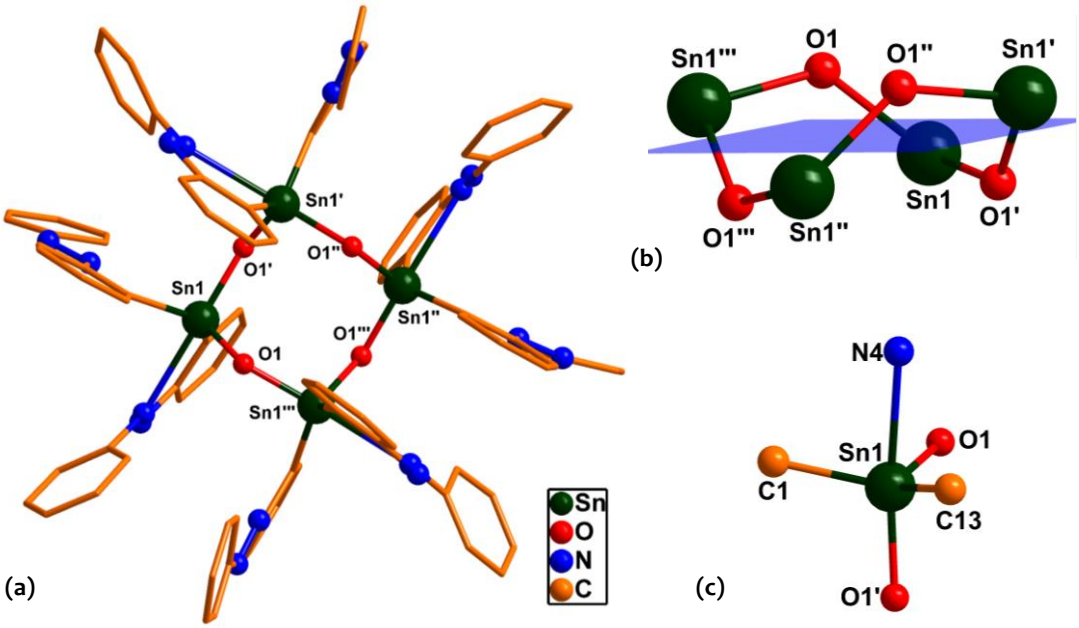

Fig. 7.9 (a) Molecular structure of complex **7**. Bond distance (Å) and bond angle (°) parameters: Sn1-O1, 1.9406(3); Sn1-O1', 1.9867(3); Sn1-O1-Sn1‴, 129.396(1)°; O1-Sn1-O1', 104.482(1)°; H atoms are omitted for clarity. **(b)** Sn_4O_4 core structure with a plane passing through no atom; **(c)** coordination environment of Sn in complex **7**; Sn1-C1, 2.1328(5); Sn1-C13, 2.1321(5); Sn1-N4, 2.6678(4); N4-Sn1-O1', 162.673(1)°, N4-Sn1-O1, 87.571(1)°; N4-Sn1-C1, 86.794(1)°; N4-Sn1-C13, 66.952 (1)°; C1-Sn1-C13, 129.258(2)°.

All the three complexes form stimulating supramolecular architectures in solid state. Complex **5** shows the formation of an interesting 1-D supramolecular chain assembled through C-H…π and C-H…N interactions, whereas two-dimensional supramolecular architecture assembled by π…π, C-H…π, and C-H…N interactions (Fig. 7.10). Complex **6** revealed the presence of π…π, C-H…π, and C-H…O interactions in the formation of 1-D supramolecular chain about the a-axis and in the formation of 2-D architecture about the c-axis (Fig. 7.11). Complex **7** forms fascinating 1-D chains and 2-D supramolecular architectures about the c-axis assembled through π…π, C-H…π, and C-H…N interactions (Fig. 7.12) [Chandrasekhar et al., 2005, 2007, 2010, 2013b; Metre et al., 2014].

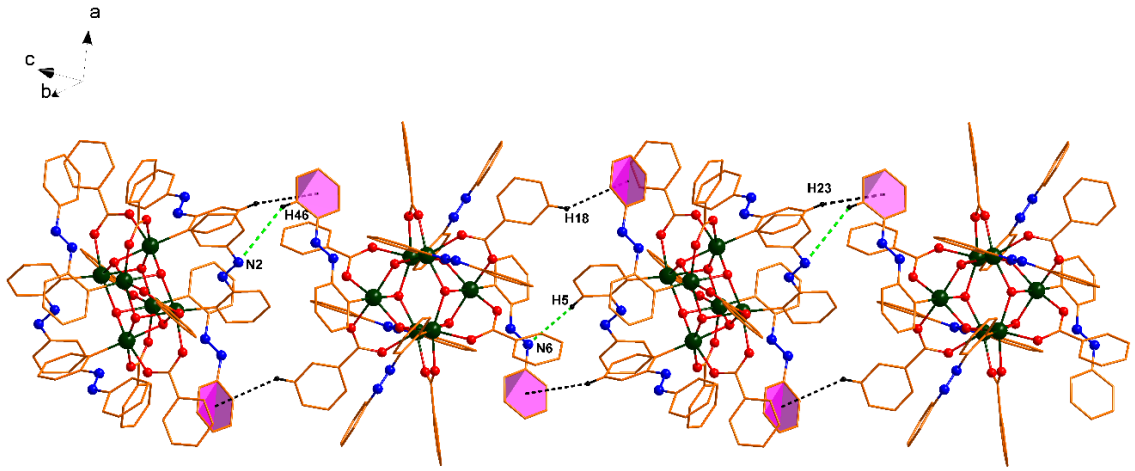

(a)

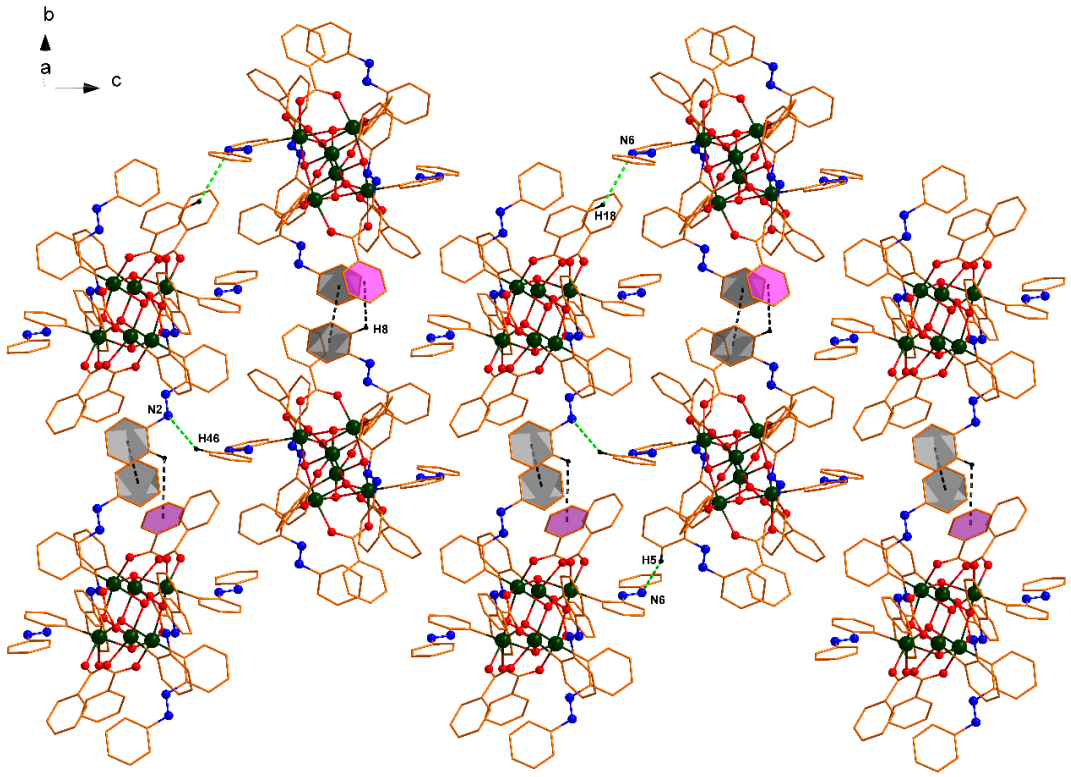

(b)

Fig. 7.10 (a) One-dimensional supramolecular assembly of **5** formed by CH…π and CH…N interactions. Metric parameters are as follows; H18-π, 3.5806(1) Å; H23-π, 3.6629(1) Å H46-N2, 3.7850(4) Å; H5-N6, 3.0071(4) Å. **(b)** Two-dimensional supramolecular architecture of **5** formed by CH…π, π…π and CH…N interactions. Metric parameters are as follows; H8-π, 3.8126(1) Å; π…π, 3.8616(1) Å; H46-N2, 3.7850(4) Å; H18-N6, 3.5772(4) Å; H5-N6, 3.0071(4) Å.

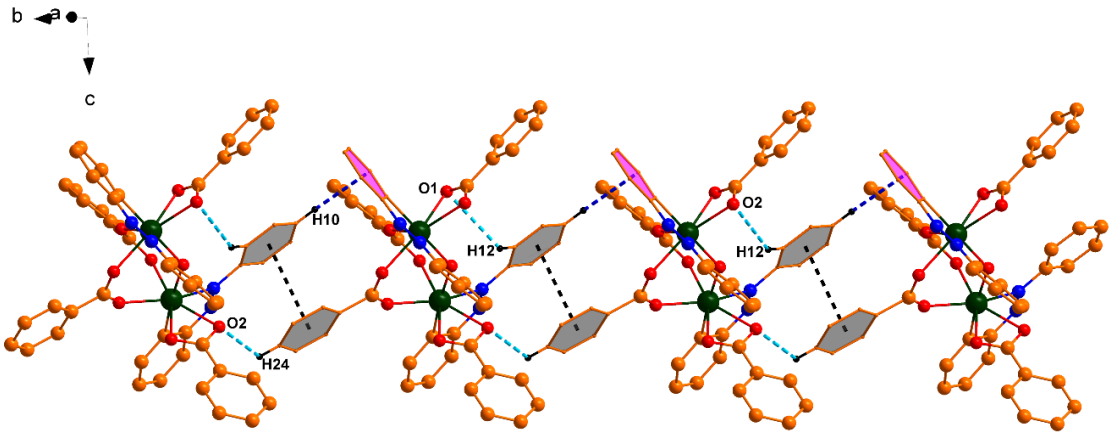

(a)

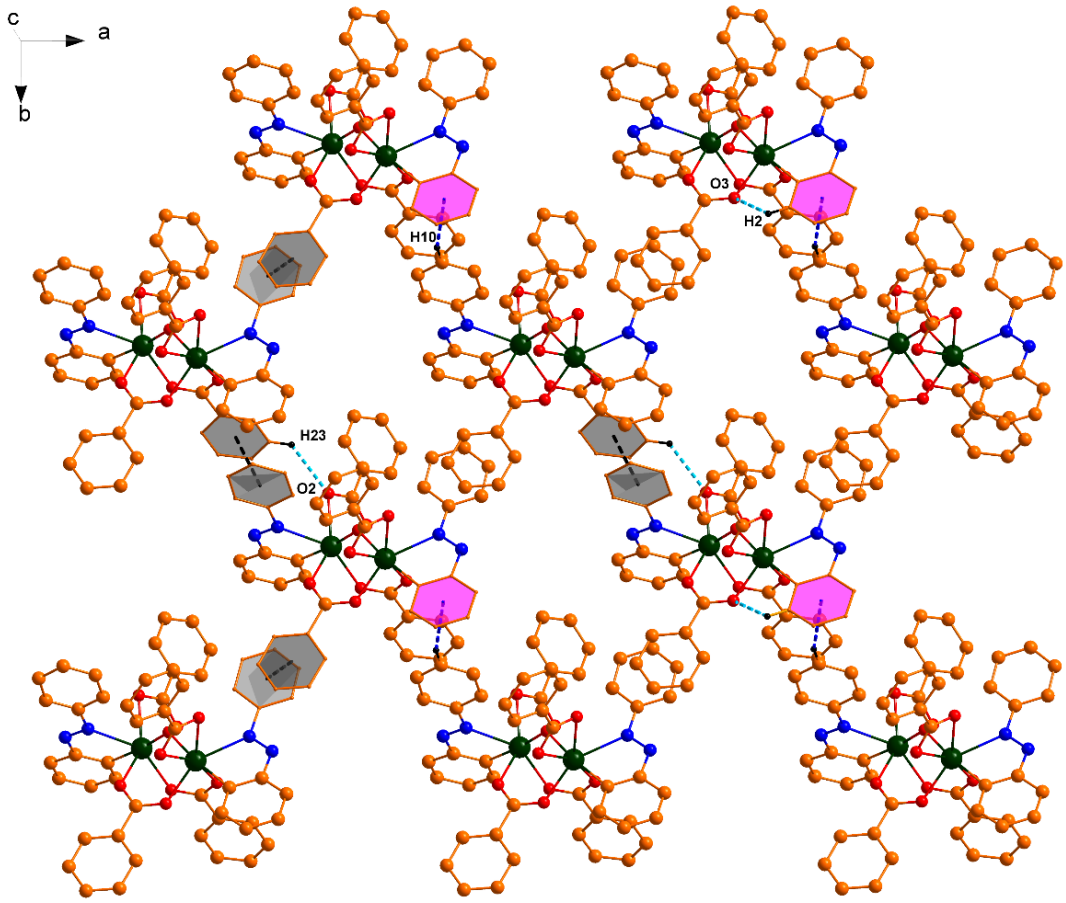

(b)

Fig. 7.11 (a) One-dimensional supramolecular assembly of **6** formed by CH…π, π…π, and CH…O interactions. Metric parameters are as follows; H10-π, 2.6680(4) Å; π…π, 3.7610(5) Å; H12-O1, 3.1452(1) Å; H12-O2, 3.4579(2) Å; H24-O2, 2.9568(2) Å. **(b)** Two-dimensional supramolecular architecture of **6** formed by CH…π, π…π, CH…O interactions. Metric parameters are as follows; H10-π, 2.6680(4) Å; π…π, 3.7610(5) Å; H2-O3, 2.7544(1) Å; H23-O2, 2.5834(1) Å.

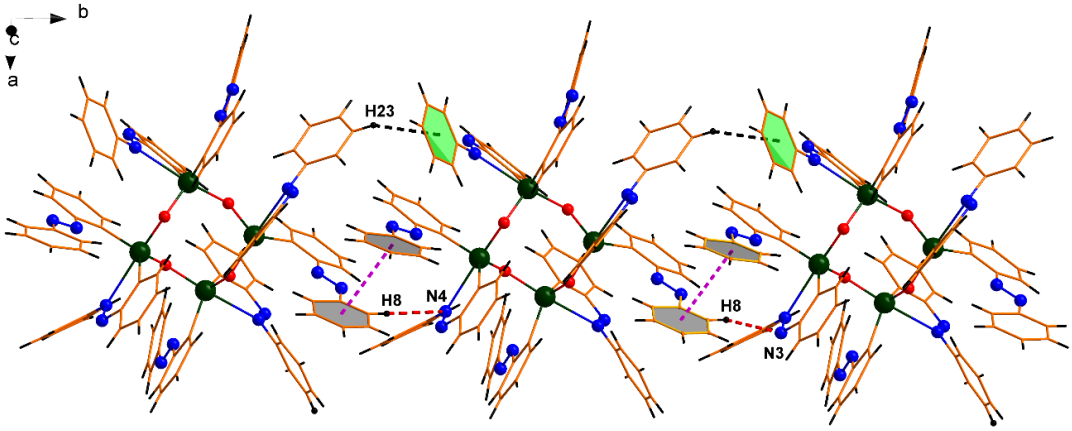

(a)

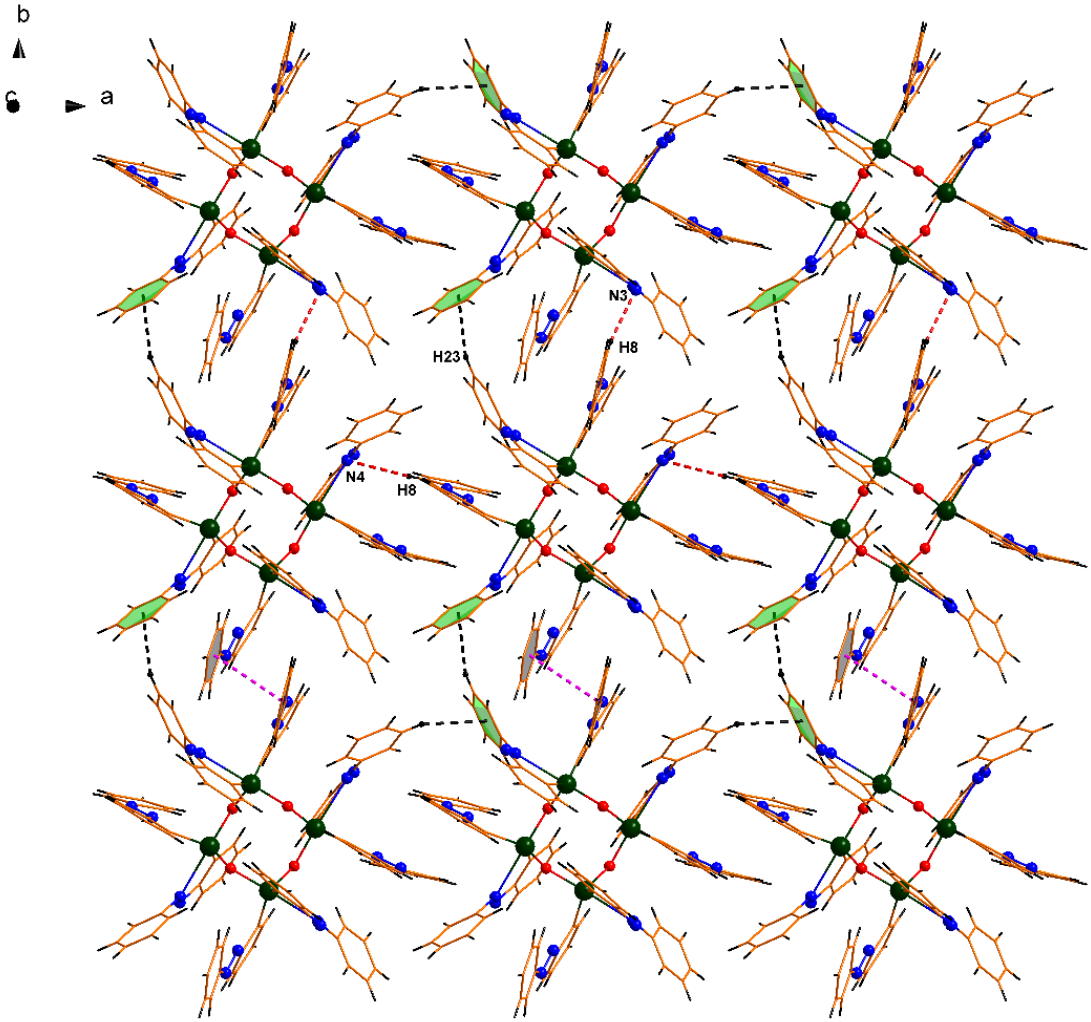

(b)

Fig. 7.12 (a) One-dimensional supramolecular assembly of **7** formed by CH…π, π…π, and CH…N interactions. Metric parameters are as follows; H23-π, 3.1509(5) Å H8-N3, 2.8275(4) Å; H8-N4, 3.5921(4) Å; π…π, 3.7587(6). **(b)** Two-dimensional supramolecular architecture of **7** formed by CH…π, π…π, and CH…N interactions. Metric parameters are as follows; H23-π, 3.1509(5) Å H8-N3, 2.8275(4) Å; H8-N4, 3.5921(4) Å; π…π, 3.7587(6).

7.3.3 Antibacterial Studies

Antibacterial assessment of complexes **5**, **6** & **7** was performed in collaboration. The antibacterial property of organotin complexes is primarily explained by Overton's concept and Tweedy's chelation theory. Overton's concept states that the lipophilicity of complexes is directly proportional to the antibacterial activity exhibited by them. The higher solubility of complexes in lipids allows them to smoothly penetrate the outer lipid bilayer of bacteria, which

in turn leads to the disruption of cellular organization [Adeyemi et al., 2019a]. Tweedy's chelation theory, on the other hand, postulates that the partial distribution of positive charge among other donor groups of complex results in the reduced polarity of the central metal ion. Moreover, the de-localization of pi-electron over the complex can further trigger the lipophilicity of the tin center [Roy et al., 2016]. All of these effects collectively catalyze the entry of complexes into the bacterial cell and result in the suppression of cell growth and metabolism. In this experiment, complex **7** exhibited higher antibacterial activity compared to that of complex **5** and **6** [Fig. 7.13-7.15]. In general, gram-negative bacteria are resistant to antibiotics and other bactericidal agents due to the presence of an additional rigid outer lipopolysaccharide coat. This extra membrane protects the bacterial cell from the invasion of any foreign agent in the cell. However, the complex **7** was equally effective against both gram-positive and negative bacteria, and the observed zone of inhibition (ZOI) was in a linear relationship with the employed concentration. Furthermore, the antibacterial activity displayed by complex **7** was comparable to standard antibiotics used in the experiment, which clearly demonstrates its future application as a potential bactericidal agent. On the other hand, the antibacterial activity measured for complexes **5** and **6** was not much significant (Table 7.2). The presence of an overall lesser organic substituent attached to the tin atom may be the reason for compromised activity shown by complexes **5** and **6** [Baul, 2008]. In addition to this, the higher steric hindrance possessed by both of these complexes may lead to the blocking of their entry into the bacterial cell.

Table 7.2 Inhibition zone of the complexes **5-7** and the antibiotic agents.

S. No.	***Antibacterial material***	***Concentration (mg/ml)***	***Zone of inhibition (mm)***	
			M. luteus	***E. coli***
1.	Complex **5**	10	NS	NS
		15	3	NS
		20	NS	NS
2.	Complex **6**	10	NS	NS
		15	4	NS
		20	NS	NS
3.	Complex **7**	10	7	7
		15	7	7
		20	8	10
4.	Ampicillin	0.1	3	4
5.	Kanamycin	0.05	2	NS

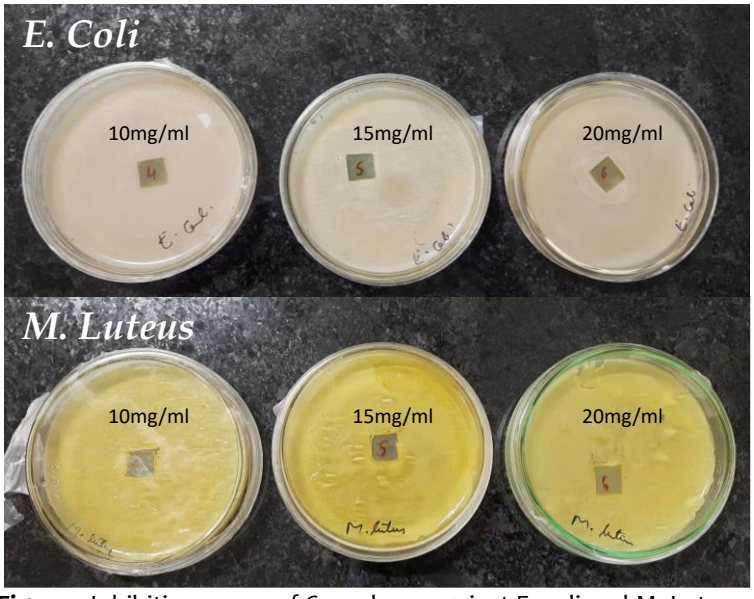

Fig. 7.13 Inhibition zones of Complex **5** against E. coli and M. Luteus.

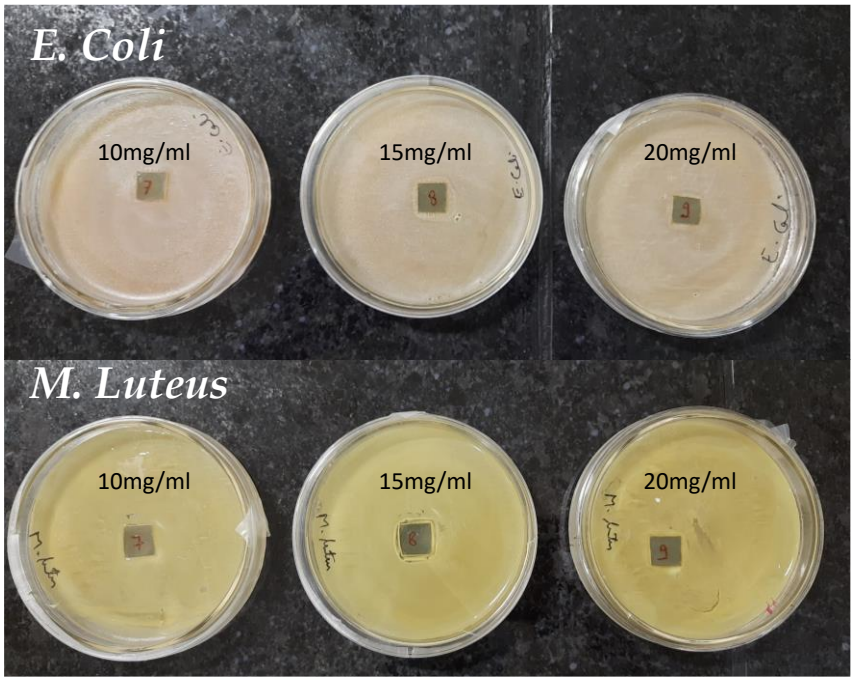

Fig. 7.14 Inhibition zones of Complex **6** against E. coli and M. Luteus.

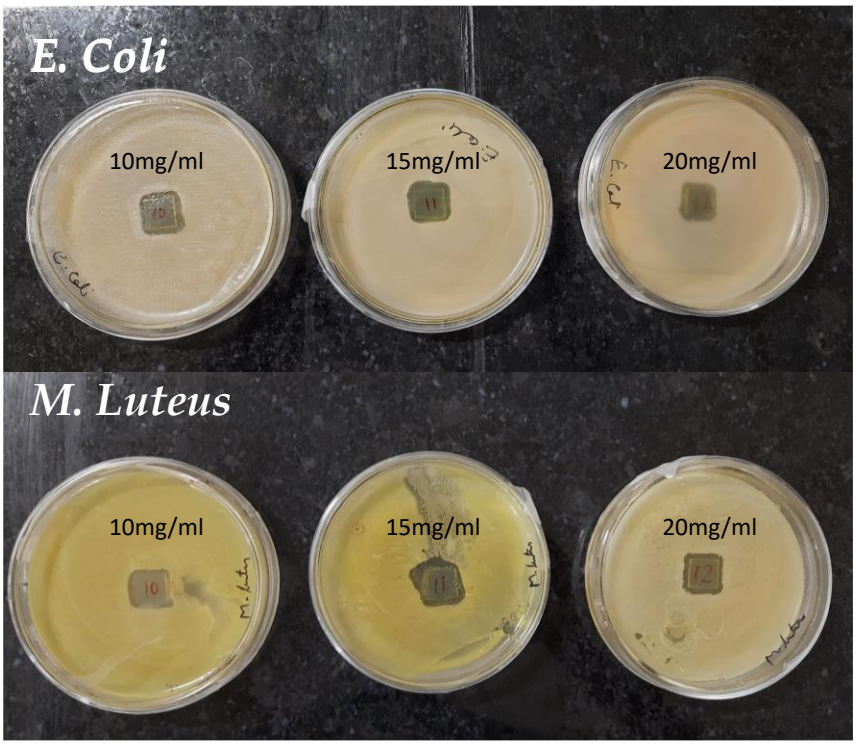

Fig. 7.15 Inhibition zones of Complex **7** against E. coli and M. Luteus.

7.3.4 DFT Studies

DFT studies were performed in collaboration. To understand the electronic nature of all the complexes **5-7**, we have performed the density functional theory (DFT) calculations using Gaussian 09 (Revision D.01) [Frisch et al., 2009]. Here, we have used the TPSSh/def2TZVP (all atoms)//TPSSh/def2SVP (all atoms) level of theory [Dirac, 1929; Mishra et al., 2020, 2021b, 2021d; Perdew et al., 2018; Slater, 1951; Staroverov et al., 2003; Tao et al., 2003; Weigend et al., 2005] for the optimization of all the three complexes. As we know that the frontier molecular orbital, such as the highest occupied molecular orbital (HOMO) and lowest unoccupied molecular orbital (LUMO) plays an important role in understanding the biological activities of complexes [Jain et al., 2020]. For complexes **5**, **6** and **7**, the HOMO energies are found to be -5.90 eV, -6.38 eV, and -5.92 eV while LUMO energies are found to be -2.89 eV, -3.24 eV, and -3.05 eV, respectively. The difference between the HOMO and LUMO energies is called as HOMO-

LUMO band gap, which is found to be 3.01 eV, 3.14 eV, and 2.87 eV, respectively for complex **5**, **6,** and **7** [Fig. 7.16]. Here, complex **7** has a lower band gap compared to complex **5** and **6,** which means in the case of complex **7**, the electronic transition is easier compared to the other two complexes [Kumari et al., 2019; Naik et al., 2020]. As the band gap increases, the complex becomes more stable, and interaction between the complex and cell decreases [Rizwan et al., 2014]. Due to this, the low band gap in complex **8** leads to the strong interaction between the bacterial cell and this complex. Based on these observations, the order of biological activity for the complexes is as follows: **7** > **5** > **6,** which is in well agreement with the experimentally observed antibacterial activities of these complexes.

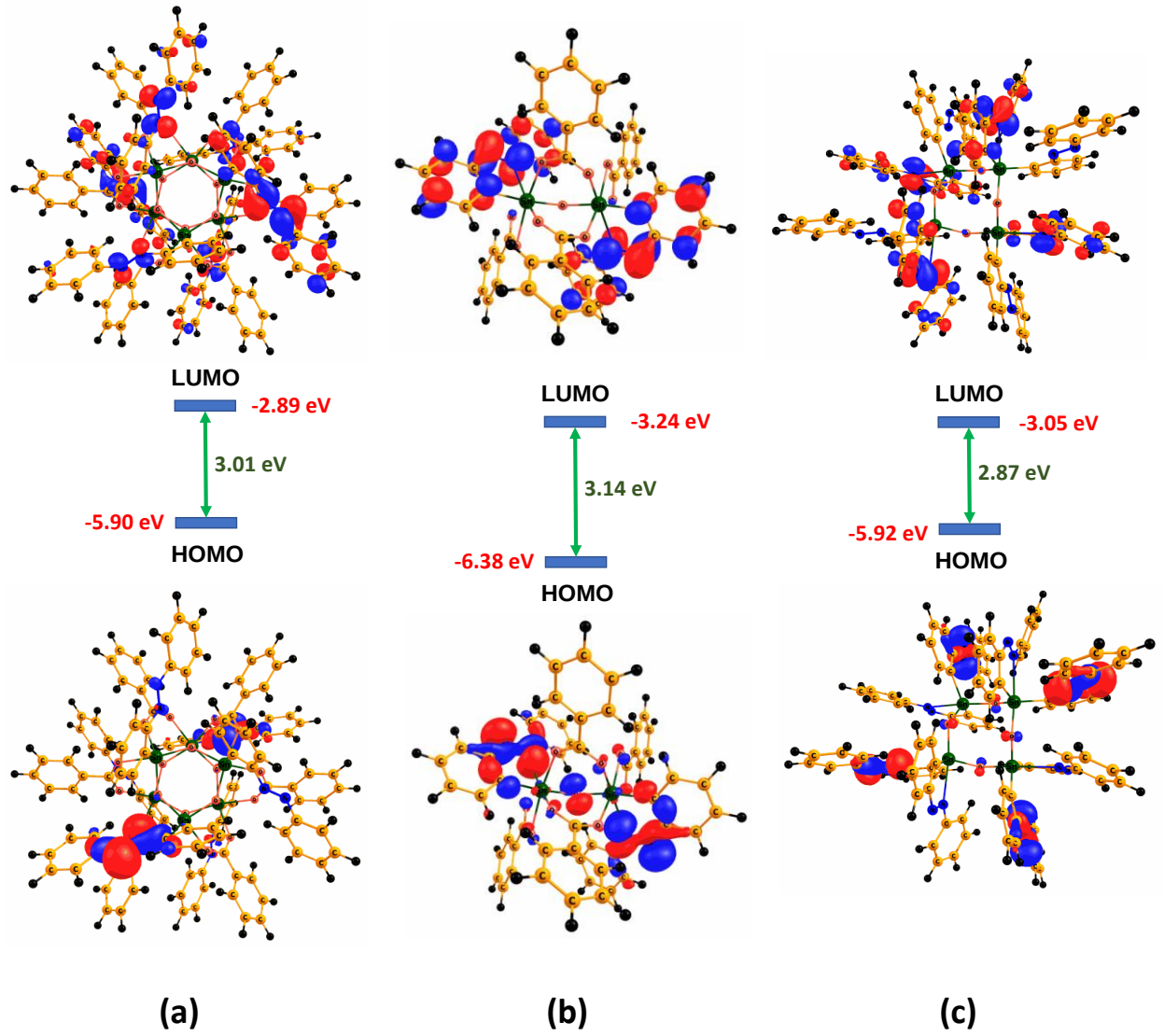

Fig. 7.16 DFT-computed HOMO-LUMO energies, gap, and their corresponding molecular orbital diagram of **(a)** complex **5**, **(b)** complex **6,** and **(c)** complex **7**, respectively. The contour value used to generate the plots are 0.03 a.u.

7.4 Conclusion

In summary, a hexanuclear monoorganostannoxane drum $[RSn(\mu_2\text{-}O)(\mu_2\text{-}O_2CPh]_6{\cdot}4PhCH_3$ **(5)**, a dinuclear monoorganostannoxane $[(RSn)_2(\mu_2\text{-}O)(\mu_2\text{-}O_2CPh)_2(\kappa^2\text{-}O_2CPh)_2]{\cdot}PhCH_3$ **(6)** and a tetranuclear diorganostannoxane macrocycle $[R_2Sn(\mu_2\text{-}O)]_4$ **(7)** (R = 2-phenylazophenyl) have been synthesized using intramolecular coordination approach, and their structures were established with single-crystal x-ray crystallography. The complexes are further characterized using Uv-vis, FTIR, ^1H, ^{13}C, ^{119}Sn NMR spectroscopy, elemental analyses, and the TGA technique. The molecular structure of the complexes revealed the hemi-labile nature of the N→Sn intramolecular coordination in complexes **5** and **7**. Single-crystal x-ray analyses revealed that the Sn center is present in different coordination environments in all the three complexes,

i.e., distorted Oh, distorted PBP, and distorted TBP geometry, respectively. Antibacterial studies were performed on these complexes, which showed the good performance of complex **7** compared to the other complexes **5** and **6**. Through the HOMO-LUMO gap analysis, it was found that complex **7** has the lowest band gap (2.87 eV), followed by complex **5** (3.01 eV) and complex **6** (3.14 eV), which is in a similar order to that observed for biological activities of these complexes.

…